Validation of the EDGES Low-band Antenna Beam Model

Nivedita Mahesh[1] , Judd D. Bowman[1] , Thomas J. Mozdzen[1] , Alan E. E. Rogers[2] , Raul A. Monsalve[1,3,4] ,
Steven G. Murray[1] , and David Lewis[1]

[1] School of Earth and Space Exploration, Arizona State University, Tempe, AZ 85287, USA; nivedita.mahesh@asu.edu
[2] Haystack Observatory, Massachusetts Institute of Technology, Westford, MA 01886, USA
[3] Department of Physics and McGill Space Institute, McGill University, Montreal, QC H3A 2T8, Canada
[4] Facultad de Ingeniería, Universidad Católica de la Santísima Concepción, Alonso de Ribera 2850, Concepción, Chile
Received 2020 October 26; revised 2021 April 13; accepted 2021 April 29; published 2021 July 1

Abstract

The response of the antenna is a source of uncertainty in measurements with the Experiment to Detect the Global Epoch of Reionization Signature (EDGES). We aim to validate the electromagnetic beam model of the low-band (50–100 MHz) dipole antenna with comparisons between models and against data. We find that simulations of a simplified model of the antenna over an infinite perfectly conducting ground plane are, with one exception, robust to changes in the numerical electromagnetic solver code or algorithm. For simulations of the antenna with the actual finite ground plane and realistic soil properties, we find that two out of three numerical solvers agree well. Applying our analysis pipeline to a simulated drift-scan observation from an early EDGES low-band instrument that had a 10 m × 10 m ground plane, we find residual levels after fitting and removing a five-term foreground model from the simulated data binned in local sidereal time (LST) average about 250 mK with ±40 mK variation between numerical solvers. A similar analysis of the primary 30 m × 30 m sawtooth ground plane reduced the LST-averaged residuals to about 90 mK with ±10 mK between the two viable solvers. More broadly we show that larger ground planes generally perform better than smaller ground planes. Simulated data have a power that is within 4% of real observations, a limitation of net accuracy of the sky and beam models. We observe that residual spectral structures after foreground model fits match qualitatively between simulated data and observations, suggesting that the frequency dependence of the beam is reasonably represented by the models. We find that a soil conductivity of $0.02\,\mathrm{S\,m^{-1}}$ and relative permittivity of 3.5 yield good agreement between simulated spectra and observations. This is consistent with the soil properties reported by Sutinjo et al. for the Murchison Radio-astronomy Observatory, where EDGES is located.

Unified Astronomy Thesaurus concepts: Radio astronomy (1338); Observational astronomy (1145); Astronomical instrumentation (799); Single-dish antennas (1460); Radio telescopes (1360); Cosmology (343); Bianchi cosmology (150); Reionization (1383); Early universe (435); Neutral hydrogen clouds (1099)

1. Introduction

Observations of the early universe spanning the first billion years, from Cosmic Dawn, when the first stars formed, to the Epoch of Reionization (EoR), when the collective radiation from galaxies influenced the entire universe, can shed light on the formation of the first stars and the thermal and ionization history of the intergalactic medium (IGM). Much useful information, such as the growth of structure, baryon densities, heating and ionization of baryons, and the physical properties of the first light sources, can be gained by studying these periods.

There are many ongoing astrophysical probes of these epochs ranging from direct to indirect techniques including Gunn–Peterson through observations toward high-redshift quasars (Fan et al. 2006; McGreer et al. 2014), tracking the evolution in the luminosity function of Lyα galaxies (Zheng et al. 2017), detection of the EoR signature in the cosmic microwave background (CMB) anisotropies (Hinshaw et al. 2013; Planck Collaboration et al. 2016); and upper limits on the "patchy" kinematic Sunyaev–Zeldovich effect (Zahn et al. 2012; Planck Collaboration et al. 2016). The redshifted 21 cm radio signal due to the spin–flip transition of the neutral hydrogen atom is of particular interest because it is a direct probe of the IGM in the EoR. The spatial and temporal fluctuations in the 21 cm signal that traces the cosmological evolution are caused by Wouthuysen–Field (Wouthuysen 1952;

Field 1958) coupling of the spin to the kinetic temperature via Lyα photons, gas heating via X-rays, and reionization via ultraviolet radiation.

There are two approaches to measuring the brightness temperature of the redshifted 21 cm signal. One approach is to statistically measure the spatial and spectral fluctuations of 21 cm emission and absorption using interferometers. Several experiments have pioneered this approach, including the LOw Frequency ARray (LOFAR; van Haarlem et al. 2013), the Giant Meterwave Radio Telescope (GMRT; Paciga et al. 2011), the Hydrogen Epoch of reionization Array (HERA; DeBoer et al. 2017), the Murchison Widefield Array (MWA; Bowman et al. 2013; Tingay et al. 2013), the 21 Centimeter Array (21CMA; Zheng et al. 2016), the Owens Valley Radio Observatory-Low Wavelength Array (OVRO-LWA; Eastwood et al. 2019), and the now decommissioned Precision Array to Probe the Epoch of Reionization (PAPER; Ali et al. 2015; Pober et al. 2015).

The second approach consists of using a single antenna element to measure the sky-averaged or "global" brightness temperature of the cosmological 21 cm signal. This method is pursued by the Experiment to Detect the Global EoR Signature (EDGES; Bowman et al. 2018, 2008; Bowman & Rogers 2010), the Shaped Antenna measurement of background Radio Spectrum (SARAS; Patra et al. 2013; Singh et al. 2017), the Probing Radio Intensity at high-Z from Marion (PRI^{Z}M; Philip

et al. 2019), the Large-aperture Experiment to detect the Dark Age (LEDA; Bernardi et al. 2016), the Cosmic Twilight Polarimeter (CTP; Nhan et al. 2018), and the now decommissioned Broadband Instrument for Global Hydrogen Reionization Signal (BIGHORNS; Sokolowski et al. 2015).

Detection of the global 21 cm signal has been limited by the interaction of the instrument with strong foreground emission. The 21 cm signal is broadband below 200 MHz and is expected to have a peak absolute amplitude between 10 and 200 mK, whereas Galactic and extragalactic continuum foregrounds from synchrotron and free–free emission are approximately four orders of magnitude larger, with typical sky temperatures of 2000 K at 75 MHz away from the Galactic center. The foregrounds generally exhibit smooth, power-law-like spectra that must be subtracted from observations to reveal the 21 cm signal. For both interferometric and global experiments, antenna beam variation with frequency, or "chromaticity," can couple angular variations in foregrounds into spectral structures, making the foregrounds more covariant with the 21 cm signal and, therefore, more difficult to separate.

In Bowman et al. (2018), we reported evidence for detection of a 21 cm global signal from the era of Cosmic Dawn using the EDGES low-band instruments. However, the absorption feature seen by EDGES was narrower and sharper than predicted and its amplitude is two to three times larger than standard astrophysical models. We considered possible alternative explanations for the observed feature, such as an instrumental artifact caused by receiver calibration errors or unmodeled frequency dependence of the antenna beam converting angular foreground power into spectral features. Others have also proposed alternative instrumental or analysis explanations (Hills et al. 2018; Bradley et al. 2019; Sims & Pober 2020) or polarized foregrounds (Spinelli et al. 2019). We conducted a number of validation tests that disfavored instrumentation effects, including repeating the measurement with multiple instruments, with the antenna at different rotation angles, and using multiple calibration solutions. We disfavored unmodeled antenna beam chromaticity by extracting the absorption feature at different local sidereal times (LSTs) when the angular structure and total power of the Galactic foregrounds were different. The EDGES high-band instrument, which uses a scaled copy of the low-band antenna, has observed at 90–190 MHz. These observations do not show a comparable structure at the scaled frequencies. They have been used to further constrain parameters of early galaxies, including UV ionizing efficiency, halo virial temperature, and soft X-ray luminosity (Monsalve et al. 2017a, 2018, 2019).

The antenna beam remains a source of potential uncertainty and error in EDGES data analysis. In order to provide estimates of the intrinsic brightness temperature of the sky, EDGES observations are corrected for the effects of the frequency-dependent antenna beam sweeping across the angular structure of the foregrounds. We use an antenna beam model and sky model to estimate these effects (Mozdzen et al. 2017, 2019). Removing this contribution from the data can introduce errors due to insufficient knowledge of the beam and sky models. We minimize errors associated with the beam by using a simple, planar dipole antenna design for all EDGES instruments, called a "blade" dipole (Oliner et al. 2007). This antenna has two advantages: it is relatively easy to simulate and, due to its compact size and simple design, its properties should change slowly and smoothly with frequency.

Motivated by the possible effects of frequency-dependent chromatic antenna beam structure on the observed spectrum and to facilitate potential improvements to the instrument design, we validate our beam models to gain better knowledge of the EDGES antenna beams and how they change with frequency. We show in Section 3.2 that for the level needed in 21 cm cosmology, the chromaticity of the beam after removing a three-term polynomial must be at the level of 0.05 (linear units) or approximately 0.01–0.1 dB across the primary response region of a dipole antenna.

There are currently no techniques available that can provide empirical measurements of a low-frequency antenna beam at the needed level. Anechoic chamber measurements typically have an accuracy of order 0.3 dB along the boresight, reducing to 0.8 dB or worse in the sidelobes (Rafique et al. 2019). This is not sufficient to characterize the fine features in the beam as needed for 21 cm cosmology. Further limiting the use of anechoic chamber measurements is that the local environment around low-frequency antennas influences their properties, necessitating in situ measurements. However, in situ measurements are very challenging. The SARAS 2 global 21 cm experiment has made in situ measurements of its antenna gain, achieving only about 10% accuracy (Singh et al. 2018). The EDGES antennas are not embedded in an array or near a large single-dish telescope, limiting the opportunities to use point-source holography (Berger et al. 2016) and drift-scan techniques (Pober et al. 2012) that rely on isolating individual point sources as they drift overhead in order to create a beam map. Transmissions from the ORBCOMM constellation of low-Earth orbit satellites have been used to successfully map antenna beams for the MWA (Neben et al. 2015; Line et al. 2018), but at 137 MHz, the transmitter frequency is above the EDGES low-band range and, at only one frequency, could not provide full frequency-dependent mapping of the beam. Drone-mounted transmitters are under development to overcome the limitations of the ORBCOMM technique and show much promise (Virone et al. 2014; Chang et al. 2015; Pupillo et al. 2015; Jacobs et al. 2017), but they have not yet demonstrated the required accuracy. Therefore, to better understand the EDGES low-band beam, we must rely on numerical simulations for the time being.

In this paper, we simulate the EDGES blade dipole antenna, used in the low-band instruments, with three different electromagnetic (EM) solvers and commercial software packages to assess the accuracy and repeatability of the simulated antenna response. In particular, the EM solvers we use are the Method of Moments, the Finite Element Method, and the Finite Difference Time Domain method. We quantify the chromatic structure in the beam and compare it with the variation seen in observations.

We begin in Section 3 with an overview of the EDGES low-band system, describe the EM Solvers we use to obtain the beam solutions, and introduce the metrics to quantify the chromaticity of the beam models. In Section 3, we present the results of modeling the antenna over an ideal ground plane with the three EM techniques. We also discuss the refinement strategies implemented to get consistent results across the different EM techniques. We use the metrics introduced in Section 3 to compare all of the beam solutions.

Section 4 shows the antenna gain results and the associated chromaticity when modeling with a finite ground plane and realistic soil beneath. These realistic beam models are used,

along with sky models, to construct simulated observations. To study the impact of the chromatic beams on observed spectra, we compare the simulated spectra with data collected using one of the low-band instruments. The spectral properties and angular distribution of astronomical radio emission are reasonably well constrained at low frequencies. In the absence of chromatic antenna beams, observed spectra should be very smooth, following the power-law shape of the dominant synchrotron and free–free emission sources. We fit and remove low-order polynomials from the simulated and observed spectra to isolate the structures introduced by the chromatic beams in the residuals. From this process, we find that the beam models yield simulated structures that qualitatively match the observations. Ultimately, however, potential errors in the beam models are difficult to separate from uncertainty in the sky model. Lastly, in this section we also confirm the electrical properties of the soil at the EDGES site by analyzing the agreement between simulated and observed sky spectra for different assumptions of the soil properties. In Section 5, we present our discussions and conclusions.

2. Methods

We use several EM solvers to obtain the response of the EDGES low-band antenna. Our goal is to calculate and analyze the chromaticity of the antenna beam pattern by obtaining beam solutions as a function of frequency. The beam pattern is used in the data-processing pipeline on the obtained sky spectra. Hence it is essential to reduce the uncertainties in the beam model that could lead to errors in data analysis. We carry out a number of simulations to cross-validate the solutions from different packages and different solvers within each package.

2.1. Electromagnetic Solvers

A variety of numerical methods exist for the analysis of electromagnetic fields associated with an antenna. They are based on the solution of Maxwell's equations or equations derived from them. Maxwell's equations are fundamental equations for electromagnetic fields and they can be solved in integral and differential form (Godara 2018). The different numerical methods can be classified based on the unknown quantity that they solve for. The solution methods and solvers we use in this analysis are as follows:

Method of Moments (MoM). The MoM solution solves for the field sources like currents and charges. These sources can be either physical sources or mathematically equivalent sources introduced through various electromagnetic field theorems (Harrington 1993). The electromagnetic fields, or the related potentials, are expressed in terms of these sources, usually through the Lorentz potentials. The expressions are integral forms, where the sources appear under some integrals, multiplied by appropriate functions, which are referred to as kernels. For example, the far fields for the EDGES antenna over a perfect electric conductor (PEC) ground in vacuum are solved with a free-space Green's function kernel for the Lorentz potentials. The MoM technique is implemented in the FEKO,[5] CST[6]—I (Integral solver), and HFSS[7]—IE (Integral Equation) software packages.

Finite Element Method (FEM). Unlike the MoM technique, FEM solves directly for the electric or magnetic field vectors, or for quantities tightly related with them (e.g., the Lorentz potentials). The starting equations are Maxwell's equations in differential form or their derivatives (e.g., the wave equation; Zienkiewicz et al. 1977). The unknowns are, hence, spread throughout the volume occupied by the fields. This volume is encompassed within a radiation box and extends up to the radiative region of the antenna i.e., the Fraunhofer distance. The FEM technique is implemented in the HFSS and CST-F software packages.

Finite Difference Time Domain (FDTD). The FDTD method employs finite differences as approximations to both the spatial and temporal derivatives that appear in Maxwell's equations (specifically Ampere's and Faraday's laws). The equations are solved in a cyclic manner: the electric field is solved at a given instant in time, then the magnetic field is solved at the next instant in time, and the process is repeated over and over again (Sullivan 2013). Because it is a time domain method, solutions can cover a wide frequency range with a single simulation run (unlike the MoM and FEM techniques), provided the time step is small enough to satisfy the Nyquist–Shannon sampling theorem for the desired highest frequency. Like the FEM technique, the FDTD solves for the *E*- and *H*-fields directly. This method therefore uses a radiation box to compute the unknowns within the enclosed volume. Of the three packages evaluated, only CST-T supports this technique.

The three techniques used across the three different commercially available software packages provide a total of six independent solutions to compare.

2.2. Antenna Model

EDGES is located in the Murchison Radio-astronomy Observatory (MRO) in Western Australia. The experiment is based on a single-element broadband radio spectrometer design. It uses multiple instruments to cover the frequency range of interest from 50 to 200 MHz. The low-band instrument operates from approximately 50–100 MHz and the high band operates from approximately 100–200 MHz. Recently, a midband instrument spanning an intermediate range of frequencies was added to the experiment.

Each instrument uses a nearly identical copy of analog and digital electronics. All instruments use a scaled copy of the same blade antenna design that has been optimized for a particular subset of the frequency range. The blade antenna is supported above a wire mesh ground plane by a fiberglass frame that has little impact on its electrical properties. The blade dipole has low beam chromaticity according to our previous simulations (Mozdzen et al. 2016). The antenna has a maximum response toward zenith, and its planar design reduces the horizon response compared to nonplanar antennas. This reduces direct pick up of ground radiation and radio frequency interference. A Roberts transmission-line balun (Roberts 1957) is used to transition from the panels to the receiver. A capacitive top plate above the blade excitation point of the antenna is employed to improve the impedance match of the antenna to the receiver. At the bottom surrounding the balun rods is a small rectangular metal shield that reduces the radiation from the vertical currents in the balun tubes, which are strongest at the base.
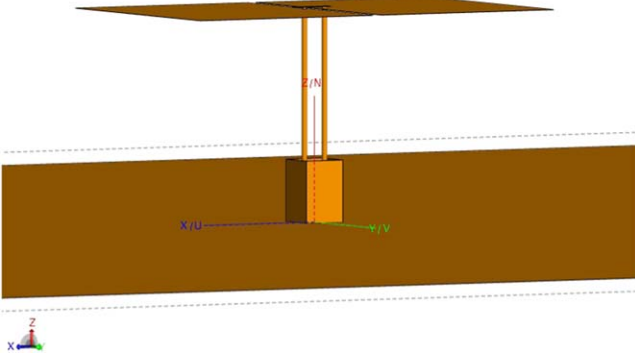

Figure 1. (Top) EDGES low-band antenna located at the Murchison Radio-astronomy Observatory in Western Australia. The panels of the blade dipole have a balun at the center that collects the signals and directs them to the receiver, which is placed below the ground plane. The fiberglass tubes (not included in the EM model) visible in the picture are used as a frame to support the panels and the balun. The center portion of the ground plane, visible in white paint, is made of metal sheets and then connects to a galvanized steel wire mesh with 5 cm grid spacing. (Bottom) Model of the EDGES antenna used in FEKO based on the dimensions in Table 1.

In this work, we will focus entirely on the EDGES low-band antenna. A photo of the low-band antenna is shown in Figure 1, and a summary of its properties is presented in Table 1.

The metal wire mesh ground plane is made from galvanized steel wires and has 5 cm of separation between mesh wires. All wires are welded at the intersections with other wires for good conductivity. The antenna and ground plane are aligned nearly north–south, with the excitation access of the antenna at an azimuth of $-7°$. Two different configurations of the wire mesh ground plane have been placed below the low-band dipole. The first deployment used a simple square of side 9.8 m. This version of the instrument acquired sky data from 2015 October through 2016 July. The ground plane was then upgraded and extended to reduce the beam chromaticity of the antenna as discussed in Section 4.2. The extended ground plane has a square mesh of side 20 m. Each side of the central mesh has four isosceles triangle extensions attached to it, evenly spaced along the edge. Each triangle extension has a base width of 4.8 m and a height of 5 m. The extended ground plane has a total edge-to-edge extent of 30 m. This version of the ground plane is used in the current low-band system and began data acquisition in 2016 September.

In our EM models, we will ignore the fiberglass support structure and treat all parts of the antenna and balun as PEC. The gain and directivity of an antenna are related by the

Table 1
Summary of EDGES Low-band Antenna Characteristics

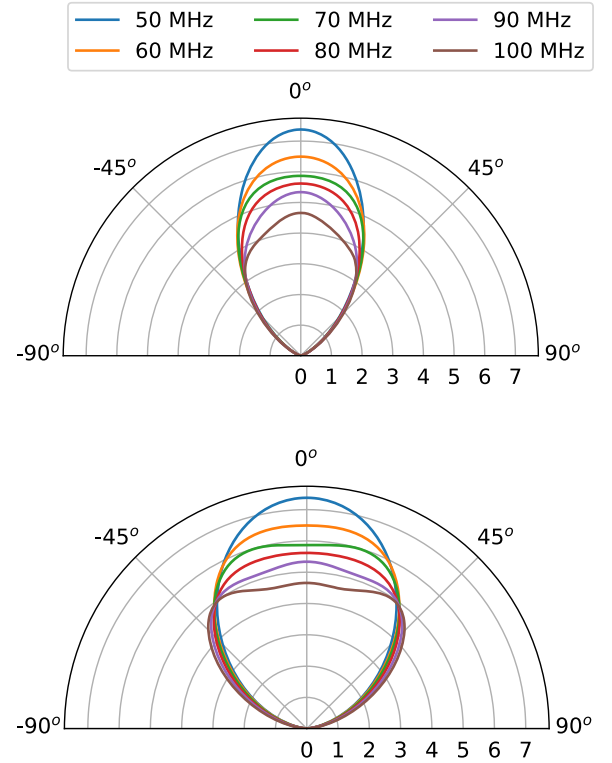| Parameter	Value
Panel length	125.2 cm
Panel width	96.4 cm
Gap between the panels	4.4 cm
Height (from the ground)	104 cm
Original ground plane	10 m × 10 m
Extended ground plane	30 m × 30 m
Ground-plane mesh grid size	5 cm
3 dB beamwidth @ 75 MHz (E-plane; $\phi = 0°$)	72°
3 dB beamwidth @ 75 MHz (H-plane; $\phi = 90°$)	110°
Excitation azimuth	$-7°$

Figure 2. Gain as a function of elevation angle (theta) for two cuts through the beam at several frequencies. The gain is plotted in linear scale. (Top) For cuts along the excitation axis of the dipole (E-plane). (Bottom) For cuts along the perpendicular axis (H-plane). These beam solutions were obtained by simulating the EDGES dipole over the 10 m × 10 m ground plane using FEKO.

antenna/electrical efficiency factor (η), i.e., $G = \eta D$. So, for a lossless antenna ($\eta = 1$) where the entire structure is modeled only with PEC as in our case, the gain and directivity will be the same. The antenna model is meshed using adaptive meshing criteria at the highest simulated operating frequency (100 MHz) in each solver, which refines the mesh until the variation in the antenna reflection coefficient (S11) between refinements converges to less than 0.1 dB. With this mesh setting, the solution for the far-field gain is calculated at 1° spacing in azimuth and elevation for frequencies between 40 and 100 MHz in 1 MHz steps. In Figure 2, we show example cross-sections of the beam gain at several frequencies. Both E-plane (along the axis of excitation; $\phi = 0°$) and H-plane (perpendicular to the axis of excitation; $\phi = 90°$) cuts of the power gain of the beam are plotted. The variation of the curves

with frequency indicates that the EDGES beam is chromatic and has to be modeled carefully.

2.3. Metrics and Figure of Merit (FoM)

We adopt two metrics to compare the beam solutions from the different solvers. These also quantify the beam variation with frequency. The first metric we use is to analyze the level of the residuals after removing a low-order polynomial fit to the gain as a function of frequency at specific azimuth–elevation viewing angles. The second metric is the derivative of the beam gain along the frequency axis:

$$\frac{G_{\theta,\phi}(\nu + \Delta\nu) - G_{\theta,\phi}(\nu)}{\Delta\nu}, \qquad (1)$$

where $G_{\theta,\phi}(\nu)$ is the gain value of the beam at a given frequency (ν) and, spherical coordinates (θ, ϕ), and $\Delta\nu$ is the small step in frequency.

We also introduce an FoM that enables us to quantitatively compare the different beam solutions in connection with our science goals. This FoM uses simulated measurements of the antenna temperature as a function of frequency obtained by convolving the antenna beam model with a sky model. For the sky model, we use the Haslam et al. (1982) all-sky brightness temperature map at 408 MHz and scale it to the desired frequency range using a spectral index of $\beta = 2.55$, following

$$T_{\text{sky}}(\nu) = T_{408} \left(\frac{\nu}{\nu_{408}}\right)^{-\beta}, \qquad (2)$$

where $T_{\text{sky}}(\nu)$ [8] is the temperature of the sky evaluated at frequency ν and T_{408} is the sky temperature from the 408 MHz Haslam sky map. At each frequency for which we have evaluated the antenna beam patterns, we project the beam pattern onto the sky map using the MRO site latitude and a specific LST. We integrate the product of the two over the sky coordinates to calculate the simulated antenna temperature at each frequency, according to

$$T_{\text{ant}}(\nu, n) = \frac{1}{4\pi} \int G(\nu, \theta, \phi) \, T_{\text{sky}}(\nu, \theta, \phi, n) d\Omega, \qquad (3)$$

where $T_{sky}(\nu, \theta, \phi, n)$ is the brightness temperature of the sky at a given frequency, spherical coordinates, and LST (n). Finally, we perform this computation in steps of 1° in LST to create a two-dimensional array of 61 frequency samples and 360 LST samples representing a simulated EDGES low-band (40–100 MHz) drift scan spanning 24 hr.

Our FoM is the rms of the residuals over the frequency range of 55 MHz to 97 MHz after fitting and removing a foreground model from each spectrum in the simulated drift-scan data. The frequency range chosen to calculate the rms excludes the band edges where the S11 of the blade antenna deteriorates quickly. The FoM (as a function of LST bin) is given by

$$\text{FoM}(n) = \sqrt{\langle [T_{\text{ant}}(\nu, n) - T_{\text{model}}(\nu, n)]^2 \rangle_\nu}, \qquad (4)$$

and we use the foreground model,

$$T_{\text{model}}(\nu, n) = \left(\frac{\nu}{\nu_o}\right)^{-\beta} \sum_{m=0}^{M-1} a_{m,n} \left[\ln\left(\frac{\nu}{\nu_o}\right)\right]^m, \qquad (5)$$

where $T_{\text{model}}(\nu, n)$ is the foreground model as a function of frequency and LST. The foreground model used is one of the models we often employ in our 21 cm signal searches. Thus, the FoM effectively captures the sensitivity of 21 cm signal searches to the antenna beam chromaticity. We refer to this foreground model, which is an approximation to the typical exponential log model used by theoretical analyses, as the LinLog model (Bowman et al. 2018; Bowman 2018). In this paper we use $M = 5$ for Equation (5).

The choice of a five-term polynomial in the FoM is motivated to yield an FoM that closely reflects the analysis that is performed to search for the global 21 cm signal. This helps us access the impact of the antenna beam on our science results. The intrinsic sky noise spectrum is dominated by Galactic synchrotron radiation ($\approx 70\%$) followed by extragalactic emission ($\approx 27\%$) and Galactic free–free emission ($\approx 1\%$) (Shaver et al. 1999). Thus, the intrinsic sky spectrum should be very smooth, following the power-law spectral shapes of these dominant emission sources. We do not expect it to contain the spectral features we see when measured through the chromatic antenna beams. This theoretical expectation motivates the use of use smooth mathematical functions to separate the intrinsic sky foreground spectrum from chromatic beam contributions in the measured data. Fitting and removing a suitable smooth function will leave residuals that depend primarily on the beam properties. We find that we need at least four terms, and typically five terms, in the polynomial to remove the features in the ideal sky spectrum (modeled without any beam effects) down to the ≈ 10 mK level where we expect to find the global 21 cm signal. Thus, if we use fewer terms, the FoM would partly quantify the ability of the polynomial fit to match the ideal sky, rather than cleanly quantify the chromatic structure introduced into the measurement by the beams. Similarly, because the smooth foreground model absorbs the large-scale trends in the spectra, the FoM is not particularly sensitive to the choice of spectral index, β, used for the sky map scaling.

We generate an FoM for the performance of the antenna pattern as a function of LST for each of the solvers. We will also use an LST-averaged FoM that is found by averaging the rms obtained at each LST bin.

3. Validation and Refinement

While we are not able to measure the beam pattern of the deployed antenna, we can measure its S11 as a function of frequency. Thus, to gain confidence that the simulations capture the actual properties of the low-band antenna, we compare its measured S11 with the simulated result from two different solvers, FEKO and HFSS-IE. All three software packages generate the same S11 values, within 0.015 (linear units), for our antenna model. This comparison is shown in Figure 3, where we see that the agreement in the absolute value of the S11 between the simulations and the measurement is within about 0.01 (limited by the adaptive meshing accuracy of the solvers). For absolute calibration of EDGES measurements for 21 cm cosmology, the antenna reflection coefficient must be known with an accuracy of 0.0003 (equivalent to about 0.01 dB) or better (Monsalve et al. 2017b). We see from
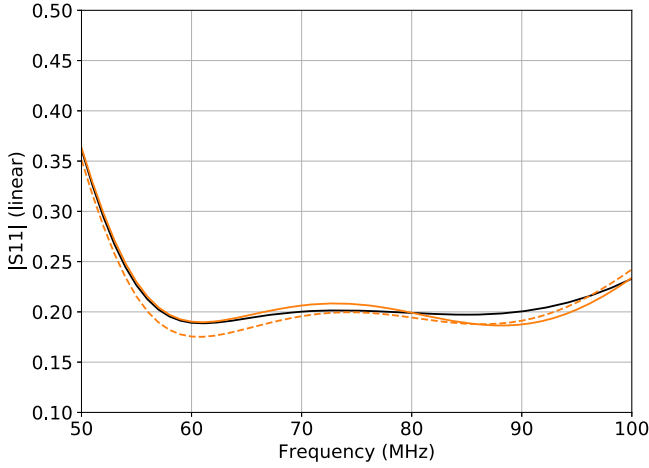
---

[8] We did not remove the contribution from the CMB to the map (2.725 K) during its frequency scaling because it is not significant for the results of this paper and because it is within the uncertainty range reported for the zero level of the Haslam map.

Figure 3. Simulated antenna reflection coefficient (S11) for the low-band antenna over the 10 m × 10 m ground plane and MRO soil below from FEKO (orange solid curve) and from HFSS-IE (orange dashed curve) compared to one day of calibrated data (2015 December 8) measured in the field (black solid curve). The agreement between the simulations and measurement is within 0.015.

Figure 3 that simulations including the real ground and ground plane in the model still do not provide sufficient agreement with the deployed antenna to rely solely on the modeling. Thus, we cannot eliminate the need for in situ antenna S11 measurements. In practice, we measure the antenna S11 in the field periodically to high accuracy (0.02 dB; Bowman et al. 2018), hence the S11 differences between measurements and EM simulations have little impact on the global 21 cm signal analysis. We also find that, while small changes to the FEKO antenna model do change the S11, they have relatively small effects on the beam compared with changing the soil parameters (see Section 4.3.3 for more discussion of soil properties). Nevertheless, the S11 simulations show broad agreement with the deployed antenna indicating they do capture the primary properties of the antenna.

3.1. Ideal Infinite PEC Ground Plane

We begin by cross-checking the results from the three packages using a simplified antenna model. Modeling the actual ground plane realistically is challenging so we first consider a model with an idealized ground plane. The antenna is modeled with its exact dimensions presented in Table 1, but instead of using the actual ground-plane dimensions and soil properties, we model the ground plane as an infinite PEC.

The far-field gain patterns obtained from each of the solvers are analyzed using the metrics discussed in Section 2.3. The antenna gain variations along the frequency for a few viewing angles on the beam are plotted in Figure 4 for each of the different solvers. As we can see, the values are found to be similar for each of the solutions. In all cases, the gain at 45° elevation is seen to be lower in the excitation plane (E-plane) compared to the perpendicular plane (H-plane). This is as expected because the total physical length of the antenna is longer along the excitation axis, implying the beamwidth will be narrow along the E-plane.

The left panel of Figure 5 shows the residuals that characterize the beam chromaticity of the EDGES low-band antenna over a PEC ground for all solvers. We see that the residuals are similar between solvers, in particular those that implement the MoM technique. The maximum deviation of the
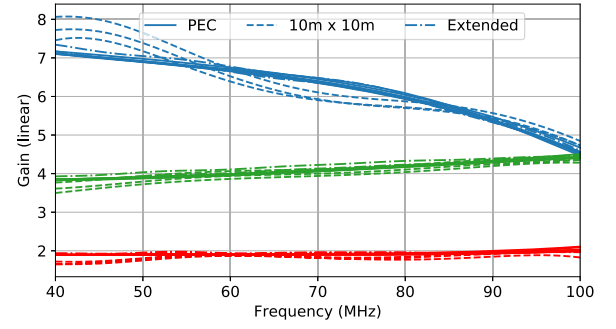

Figure 4. Antenna beam gain as a function of frequency for the three ground-plane cases: PEC (solid), 10 m × 10 m (dash), and extended (dashed–dotted). Each ground-plane case is shown at three viewing angles: zenith (blue), 45° elevation along the E-plane (red curves), and 45° elevation along the H-plane (green curves). The gain curves from all of the EM solvers are shown (but not labeled individually). In most cases the solutions from the different EM solvers overlap at the resolution of this plot, although some differences are apparent in the 10 m × 10 m solutions. As expected, the PEC and extended ground-plane cases are more similar.

gain from a regular three-term polynomial fit is found to be about 0.008 (linear units) for all cases except from the FEM solvers, in which case it is about 0.015 (linear units). The plots in Figure 6 show the frequency derivative of the gain at specific viewing angles as introduced in Equation (1). We see that the gain derivative plots from FEKO, CST-I, and HFSS-IE are qualitatively similar.

3.1.1. Compensating for Fine Structure in HFSS-IE Models

We found high-order variations with frequency in the residuals from the HFSS-IE solver (see Figure 7) and attribute them to numerical artifacts due to a lower accuracy of the solver. To compensate for this excess structure, we fit a regular six-term polynomial ($\sum_{n=0}^{n=6} p_n x^n$) in frequency at every sampled azimuth–elevation point in these solutions and use the resulting fits in place of the original solutions. The HFSS-IE panels in Figures 4–6 show the results after following this procedure. They qualitatively match the solutions from the other solvers. Other than the raw output from HFSS-IE shown in Figure 7, the analyses of all HFSS-IE beam patterns presented in this manuscript have been performed on polynomial-filtered beam patterns.

3.1.2. Radiation Box and Meshing Refinement in FEM Models

In HFSS, the antenna was initially simulated using the Absorbing Boundary Condition (ABC) on the radiation box with different padding distances from each of the model edges. On varying the radiation box size, the gain was also seen to vary (Figure 8). This dependence of the gain solution on the radiation box size, combined with larger chromaticity than any of the MoM solutions, suggested that the effects were caused by the solver and not inherent in the antenna. This issue was solved by using a Perfectly Matched Layer (PML) boundary setting instead of the ABC radiation box. A PML boundary ensures nearly zero reflection at the radiation boundary, making the far-field solutions independent of the box size. The solutions obtained after using a PML boundary are used in Figures 4–6. This solution looks qualitatively similar to the MoM solutions. The CST-F solver also requires a bounding box around the EM structure. With the same reasoning as noted
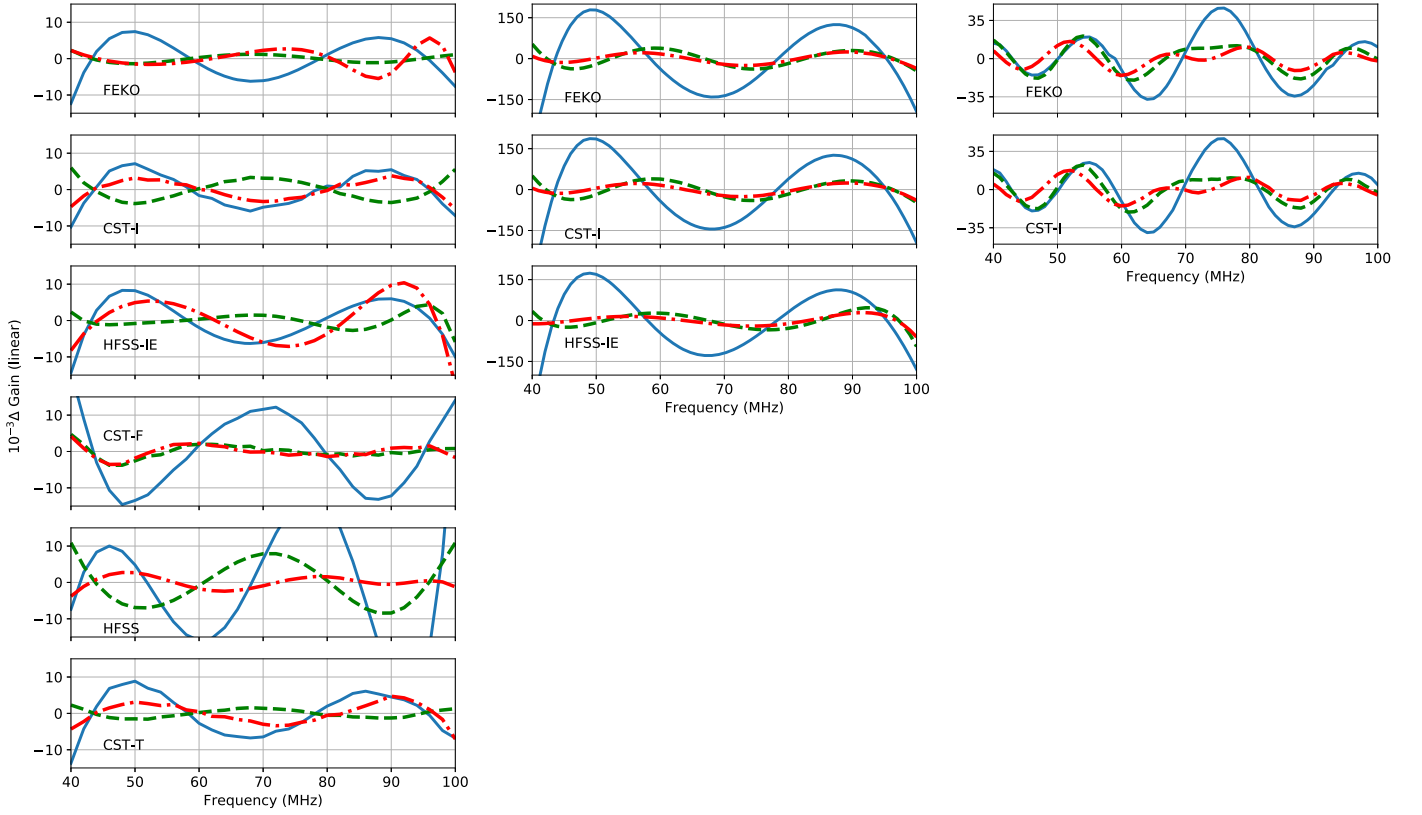
Figure 5. Residuals after fitting and subtracting a regular three-term polynomial in frequency to the antenna beam gain along three example viewing angles for each solver and ground-plane case: (left) PEC, (middle) 10 m × 10 m, and (right) extended ground plane. For each model all the available simulation solutions are shown. The residuals are calculated for the gain curve at zenith (blue solid), 45° elevation along the *E*-plane (green dashed), and 45° elevation along the *H*-plane (red dashed–dotted). The maximum level of chromaticity for the PEC ground is the lowest among all the three cases at a level of ≈0.010. The 10 m × 10 m shows a maximum deviation of 0.15, and the extended shows an improvement with the level of the residuals of ≈0.040.

for the HFSS simulation, a PML boundary was used in the CST-F simulation.

The solutions from the CST-F models were further seen to vary based on the initial mesh setting. This was the case even though we adopted adaptive mesh settings, as we did with every solver. We increased the mesh cells until the obtained solutions were independent of the mesh size. In CST-F, this was achieved at a higher mesh density of $\lambda/20$ seed mesh size compared to $\lambda/8$ for the HFSS model. The factor of 2.5 difference which implies 2.5^3 more cells in CST-F and that the latter required a bounding box padding of $\lambda/3$ (versus $\lambda/4$ used by HFSS) resulted in the highest number of mesh cells (∼4.6 million) used for the CST-F simulation among all solvers. This also translated to needing 16× more memory. The analyses of CST-F beam patterns presented in this manuscript have been performed on simulations with the PML boundary and higher seed mesh setting. In Table 2 we summarize the performance properties of each of the EM solvers as configured for our models. The corresponding gain derivative plot is shown in Figure 6 and is in agreement with the solutions from the other solvers.

We also note that the FDTD solver, CST-T, uses a PML boundary for the radiation box by default for determining the far-fields. Like the CST-F solver, this solution method also required a denser seed mesh setting. This was expected as the FDTD technique is known to be computationally intensive in terms of memory and time (Schneider et al. 2002).

3.2. Best-case FoM

For the idealized infinite PEC ground-plane test model, the FoMs derived from each of the EM solvers are shown in Figure 9. They all follow a similar trend, each peaking when the Galactic center is near zenith (LST ≈ 18 hr) and reaching a minimum when the Galactic center is not visible or is low on the horizon (LST ≈ 6 hr). For all the solutions, the FoM reaches a minimum of about 40 mK. The solvers all yield a maximum when the Galactic center is in the beam, although the values range from 100 to 500 mK and the relative position of the maximum varies.

In Table 2, we show the LST-averaged FoM for each solver. We see that solutions from all the solvers and methods, except for those from HFSS, are in good general agreement and do not vary by more than 25%. The beam solutions from HFSS indicate higher chromaticity. Given the similarities between the other solvers, this can be attributed to a low numerical accuracy of HFSS, and in particular of HFSS-IE (as noted in Section 3.1.1). We also see that the chromaticity level of 0.01 (shown in Figure 16) of the EDGES low-band blade antenna over PEC ground results in an antenna temperature residual spectral structure of 65 mK on average and as good as <30 mK at some LSTs (Figure 9). This generally meets the needs for 21 cm cosmological experiments searching for a signal of order ≈100 mK, even without applying any beam corrections during analysis. While the idealized infinite PEC ground plane yields a best-case FoM given the EDGES antenna design, we will see in the next section that the extended ground plane performs nearly as well.
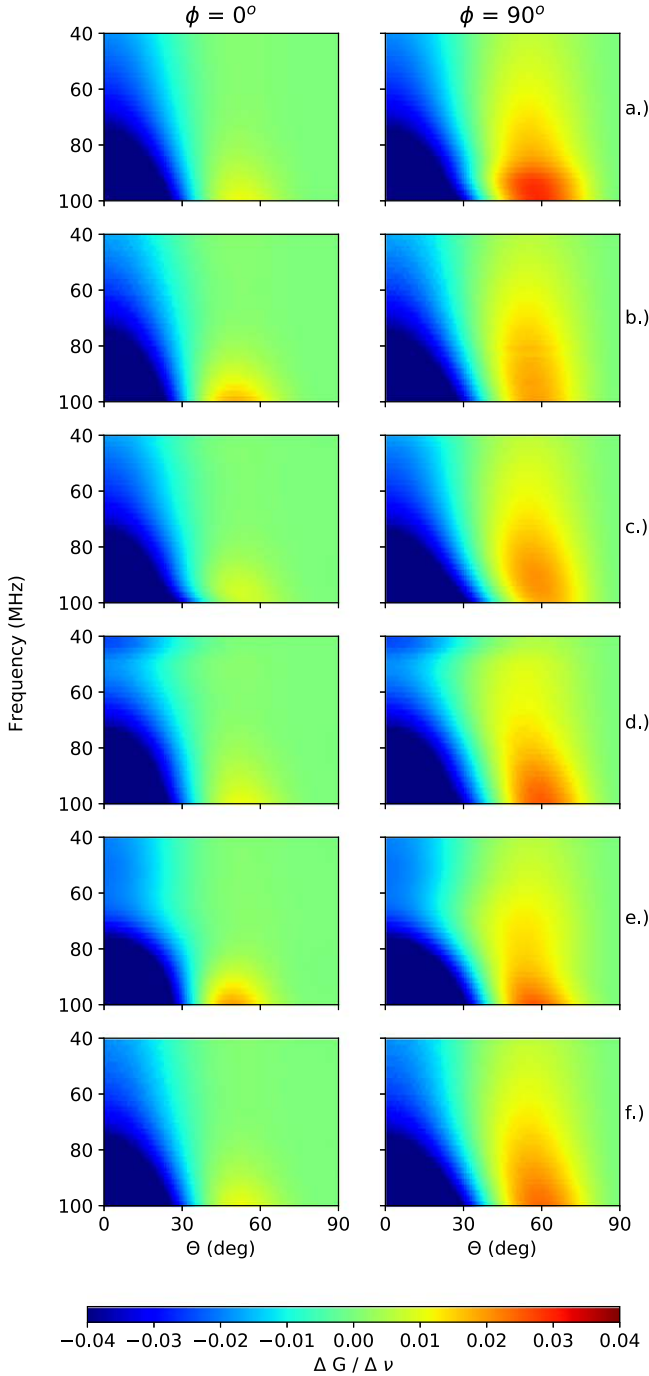
Figure 6. Change in gain per MHz as a function of elevation angle along the *E*-plane (left) and *H*-plane (right) for the EDGES low-band dipole placed over an infinite PEC ground. Each row shows the result from a different solver: (a) FEKO, (b) CST-I, (c) filtered HFSS-IE solution, (d) CST-F, (e) HFSS, and (f) CST-T.

Figure 7. Change in gain per MHz as a function of elevation angle along the *E*- and *H*-plane for the blade dipole placed over an infinite ground (PEC) modeled using (top) the HFSS-IE solver and (bottom) HFSS-IE solution with a regular six-term polynomial fit.

4. Results

In Section 3, we verified that the simulated beam pattern and chromaticity of the blade antenna over an ideal PEC ground plane are consistent between the three different EM simulation techniques and three independent software packages. However, our idealized model with an infinite PEC ground plane represents a best-case scenario. In reality the ground plane will have a finite size and the currents will reach the actual soil below the ground plane, creating additional frequency-dependent structure in the beam patterns. We now proceed to simulate realistic soil below the antenna structure along with the actual, finite ground planes used by EDGES. The EM solvers that have the capability to simulate an infinite dielectric ground are those that are based on the MoM technique. They are FEKO, HFSS-IE, and CST-I.

4.1. Realistic Soil and 10 m × 10 m Ground Plane

We begin by modeling the original ground plane for the low-band antenna, which was a 10 m × 10 m square made from metal wire mesh, as described in Section 2.2. To reduce the complexity of the EM simulations, we model the ground plane as a finite PEC solid plate, rather than as a mesh. The soil below the ground plane is included as a half-space boundary condition (i.e., it is infinite in $\pm X$, $\pm Y$, and $-Z$ directions). In this case, the MoM solver engine uses a different Green's function kernel for the lossy dielectric media in the $-Z$ hemisphere than for the free-space above. For the soil properties, we use a conductivity of $\sigma = 0.02 \, \mathrm{Sm}^{-1}$ and a relative permittivity of $\epsilon_r = 3.5$. These values were measured by Sutinjo et al. (2015) for samples of soil from the MRO.

The solutions for the derivatives of the gain across frequency are plotted in Figure 10. In the plots we see that the realistic finite ground-plane solutions have more structure in frequency than in the ideal ground case (Figure 9). There is good qualitative similarity in the beam chromaticity between the three real ground simulations, thus giving confidence that this structure is real. The dashed lines in Figure 4 show the absolute gain variations along a few viewing angles on the beam patterns. The residuals to a three-term polynomial across frequency to each of the curves for the finite ground-plane model show larger fluctuations than the ideal ground case (see Figure 5). The maximum peak-to-peak residual across
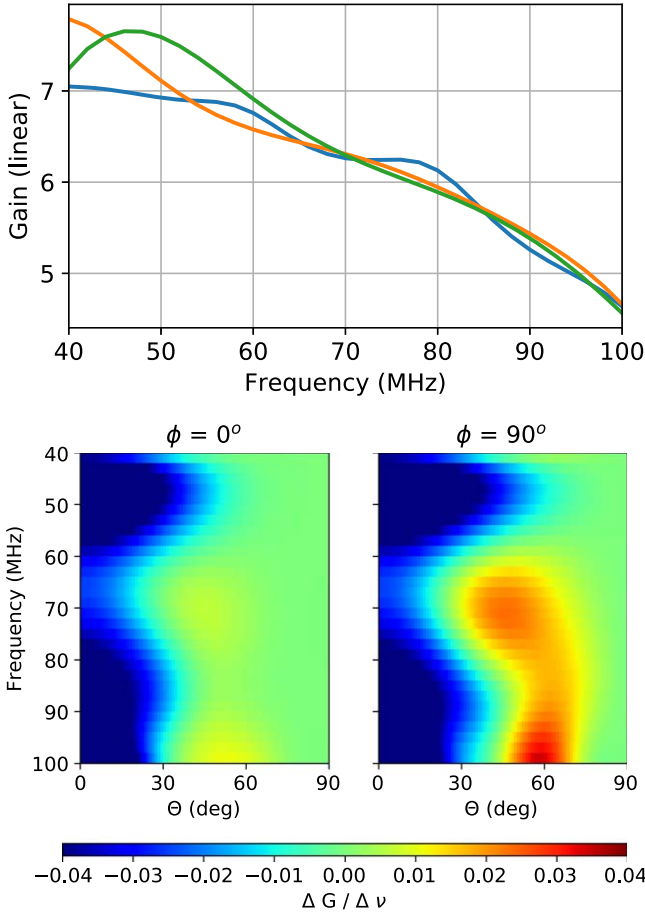
Figure 8. (Top) Zenith gain as a function frequency obtained from HFSS simulations for different radiation box sizes with Absorbing Boundary Condition. The blue, orange, and green curves represent $\lambda/1.5$, $\lambda/3$, and $\lambda/4$ box paddings, respectively. The gain varies with box size and does not converge even for a large value of padding such as $\lambda/1.5$. (Bottom) Change in gain per MHz as a function of elevation angle along the E-plane (left) and H-plane (right) for the blade dipole placed over an infinite PEC ground below and a surrounding ABC type radiation box which is modeled using HFSS solver. This gain variation is larger than any of the solutions shown in Figure 6.

frequency is about 0.2 (linear units), compared to 0.008 for the ideal ground. Good agreement is seen between the solutions from the three solvers. Quantitatively, the higher chromaticity results in a larger value for the FoM compared to the ideal ground case, as can be seen in Figure 9. The FoM peaks at about LST ≈ 18 hr with a value of 1 K and drops to 20 mK at LST ≈ 5.5 hr. The LST averages of these FoM values are summarized in Table 2 and are of the order of ≈250 mK which is about 3.5 times larger than the ideal ground case. The CST-I and FEKO solutions agree to 13.4%. Similar to the PEC case, the HFSS-IE result is significantly higher.

4.2. Extended Ground Plane

We showed above that the original square $10\,\mathrm{m} \times 10\,\mathrm{m}$ ground plane used for the EDGES low-band instrument resulted in the LST-averaged FoM for the simulated antenna spectra being in the range 212–292 mK, whereas we expect the lowest chromaticity that we could achieve with a blade planar dipole should approach the ≈65 mK limit of the ideal ground case shown in Section 3. Improving the performance of the ground plane beyond its original design was important to meet the science objectives. With the objective of achieving an LST-

averaged FoM below 100 mK, we conducted a design study aiming for a factor of 2 improvement. In order to decrease the chromaticity, we must reduce the contribution of the reflected waves from the soil to the main beam response. This involves reducing the currents that reach the soil, which can be done by increasing the ground-plane size and/or modifying its shape.

We simulated and analyzed different sizes and a few possible shapes of the ground plane using FEKO in order to identify designs that achieved our goal. In addition to simple square ground planes, we included plus-shaped designs and squares with triangular "sawtooth" extensions around the perimeter. Among the designs tested, we simulated plus-shaped ground planes of maximum length 15 m and 30 m. The 15 m and 30 m sized plus ground planes are made of five sections of $5\,\mathrm{m} \times 5\,\mathrm{m}$ squares and $10\,\mathrm{m} \times 10\,\mathrm{m}$ squares, respectively. The sawtooth designs, with a central square and triangles along the perimeter, were similar to the extended ground plane described in Section 2.2, but with varying square sizes in the center. The plus-shaped and sawtooth configurations were considered based on the analysis done in Meng Donglin & Li (2015), which showed that more edges along the perimeter of the ground plane reduce the reflection from the surrounding soil. The designs and shapes of the ground plane we explored were planar to avoid horizon response. The resulting FoM values are listed in Table 3.

Three main conclusions that can be drawn from the table are as follows: (i) for a given shape, the larger the area, the lower the FoM, (ii) for roughly the same area, the FoM of the sawtooth design is lower than the FoM of the plus shape, which in turn is better than the FoM obtained from the square ground plane, and (iii) for the same area of the sawtooth ground plane, increasing the number of edges beyond 16 (by increasing the triangles used) did not affect the FoM significantly. A higher number of edges reduces the currents that reach the soil, which in turn helps to reduce the beam chromaticity. The plus-shaped and sawtooth ground planes also have the added advantage that they require less metal for a given tip-to-tip extent.

Based on this analysis, we arrived at the final design for the larger ground plane of $20\,\mathrm{m} \times 20\,\mathrm{m}$ square with triangle extensions described in Section 2.2 and shown in Figure 11. The extended ground plane was simulated in FEKO and CST-I. We do not present solutions from HFSS-IE because the beam solutions could not be filtered with a six-term polynomial in frequency to remove the solver errors (as described in Section 3.1.1) without smoothing structures that were part of the actual beam response. The beam derivative plots of FEKO and CST-I solutions are shown in Figure 12. We can see that, as expected, the extended ground plane produces more structure than the ideal ground, but at smaller frequency scales than the original $10\,\mathrm{m} \times 10\,\mathrm{m}$ ground plane. Overall, the reduction of large-scale fluctuations in frequency improves the chromaticity. This is also shown in the right column of Figure 5, where the residuals of the gain to a regular three-term polynomial are below 0.04—more than a factor of 5 improvement over the residuals produced by the original $10\,\mathrm{m} \times 10\,\mathrm{m}$ ground plane. The solutions for the derivatives of the gain across frequency are plotted in Figure 12. In the plots we see that the extended ground-plane solutions have more structure in frequency than in the ideal ground case (Figure 9) but are more gradual compared to the $10\,\mathrm{m} \times 10\,\mathrm{m}$ case. There is good qualitative similarity in the beam chromaticity between the FEKO and CST-I simulations, thus giving confidence that

Table 2
Comparison of EM Solvers

Solver	Technique	Mesh Cells[a]	Memory[a]	LST-averaged FoM[b]		
				PEC[c]	10 m × 10 m[d] Ground Plane	Extended[e] Ground Plane
		(#)	(MB)	(mK)	(mK)	(mK)
FEKO	MoM	2262	103	61.8	240 (0)	82 (0)
CST-I	MoM	5964	1556	63.3	212 (54)	101 (40)
HFSS-IE	MoM	5210	310	109.0	292 (77)	...
CST-F	FEM	4654,080	16,055	50.7	...	...
HFSS	FEM	15,102	1231	84.0	...	...
CST-T	FDTD	926,478	1257	68.0	...	...
Actual Data	...	...	...	...	280 (188)	130 (120)

Notes.
[a] Determined for an ideal ground plane (PEC).
[b] For the real ground cases, the FoM after applying a beam correction to the simulated and actual observations is indicated in parentheses. The beam correction is calculated as in Mozdzen et al. (2017, 2019) using the sky model and the FEKO model for all cases. As expected, the beam correction removes all of the residual structure when applied to the simulated observations from the FEKO beam model. It also substantially lowers the FoM for the simulated observations generated by the other solvers, indicating their beam patterns are similar to the FEKO patterns. When applied to the actual data, we see that the beam correction lowers the FoM by 33% for the 10 m × 10 m ground plane and 8% for the extended ground plane.
[c] Section 3.1.
[d] Section 4.1.
[e] Section 4.2.

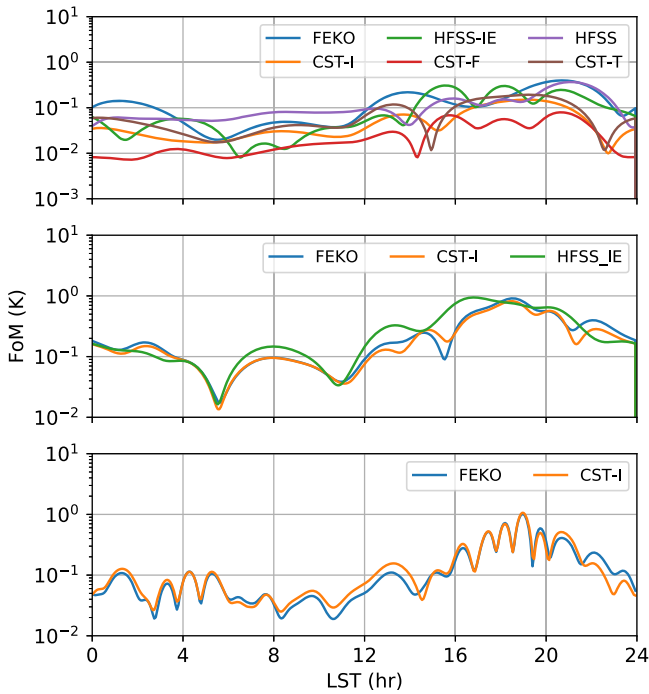**Figure 9.** FoM as a function of LST for the three ground-plane cases: PEC (top), 10 m × 10 m (middle), and extended (bottom). All the available beam solutions from different solvers are shown. The FoM was calculated with Equation (4) and using a five-term LinLog model for the spectrum (Equation (5)).

Figure 10. Same as Figure 6, but for the 10 m × 10 m ground-plane case and using only the Method of Moments solvers: FEKO, CST-I, and HFSS-IE. This gain variation plot is seen to have more structure compared to the PEC case.

this structure is real. The FoM versus LST plots show that the rms of the residuals never exceed 1 K for both FEKO and CST-I solutions and is as low as 20 mK when the Galactic plane is below the horizon. The average FoM across LST with the extended ground plane obtained from FEKO is 82 mK and from CST-I is 101 mK (a difference of 22%). The 10 m × 10 m and extended cases have roughly the same FoM when the Galactic center is near zenith, but the extended cases go to a lower FoM at low LST for a longer period of time.
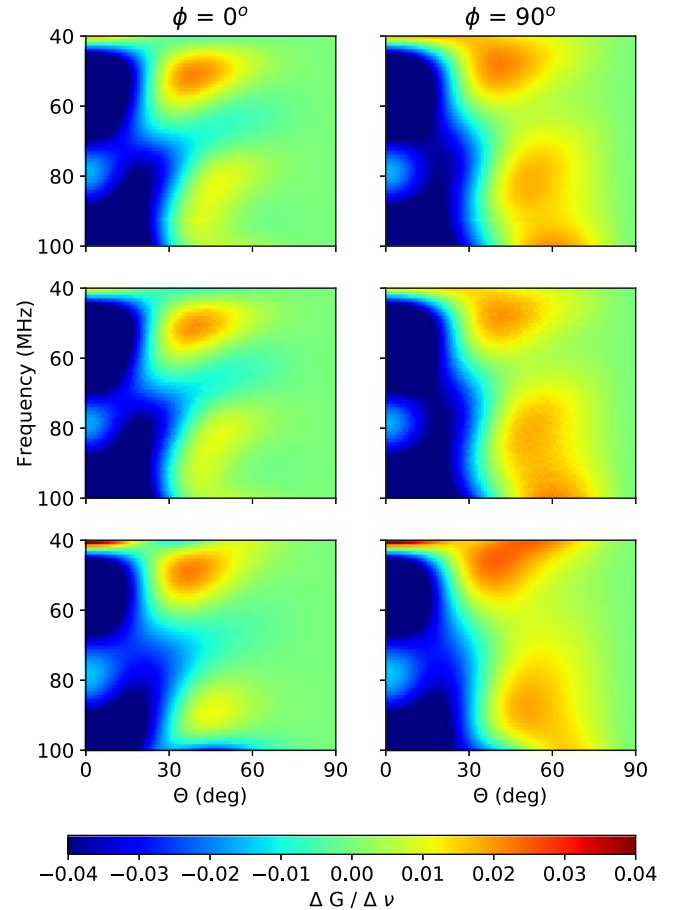
Table 3
Comparison of the Figure of Merit (FoM) for Different Cases of Finite Ground Planes Modeled with FEKO

Size (m)	Shape	Area (m^2)	LST-averaged FoM (mK)
10	Square	100	213
20	Square	400	205
30	Square	900	192
15	Plus	125	255
30	Plus	500	181
10 (8)	Sawtooth	200	151
15 (12)	Sawtooth	375	149
20 (16)	Sawtooth	600	80
20 (20)	Sawtooth	600	90

Note. For the sawtooth designs, the size listed is the dimension of the inner square region. The number of triangles added around the perimeter of the inner square is listed in parentheses. The added triangles have 5 m base and 5 m height in all cases except for the bottom row, for which the triangles had 4 m base and 5 m height.
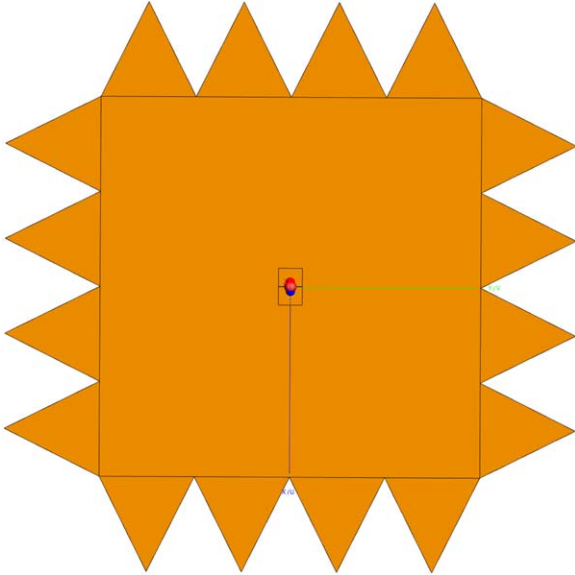
Figure 11. Rendering of the extended ground plane. It consists of a central square metal plane that is 20 m × 20 m. Each side has four isosceles triangles that are each 5 m at their base and 5 m long to their tip. The overall size of the ground plane is 30 m × 30 m. In the field, the width of each of the isosceles triangles is slightly narrower than 5 m (4.8 m). This is due to the size of the mesh sheets we used to build the actual ground plane.

4.3. Comparison with Data

In the previous sections, we have found that the beam solutions for four out of the six solvers tested agree to within 25% for an ideal ground-plane case and that the MoM solvers agree to within 20% for finite ground-plane cases. Here we assess the overall accuracy of the beam solutions by comparing simulated observations to actual data.

We use data collected from the EDGES low-band (low-1) instrument with both its original 10 m × 10 m ground-plane configuration and its later extended 30 m ground plane. The data with the original ground plane spans the days 2015-286 to 2016-186 and with the extended ground plane 2016-258 to 2017-95. The raw data are cleaned for RFI and corrected for the calibrated receiver response. The data-reduction pipeline we used here is similar to what was done with other EDGES data
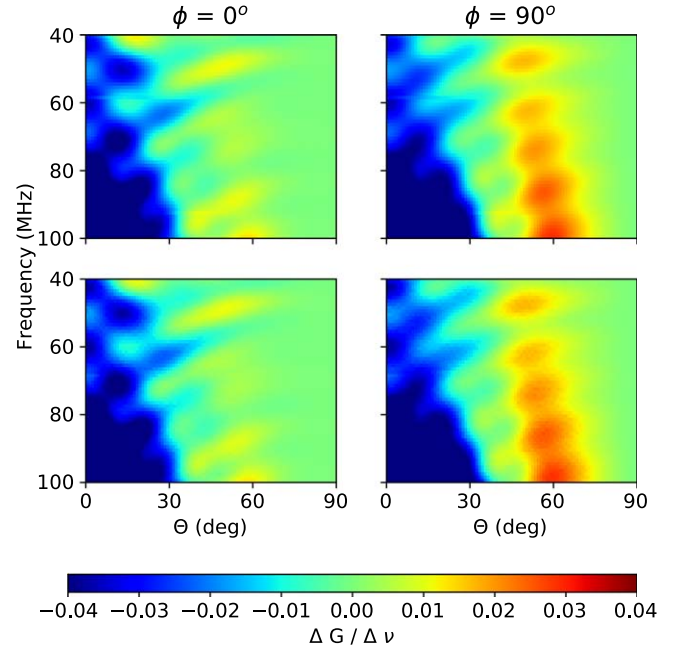

Figure 12. Same as Figure 6, but for the extended ground-plane case using the solutions from FEKO and CST-I. Along each viewing angle, the variation of the gain with frequency is more gradual compared to the 10 m × 10 m ground plane but larger than the PEC case.
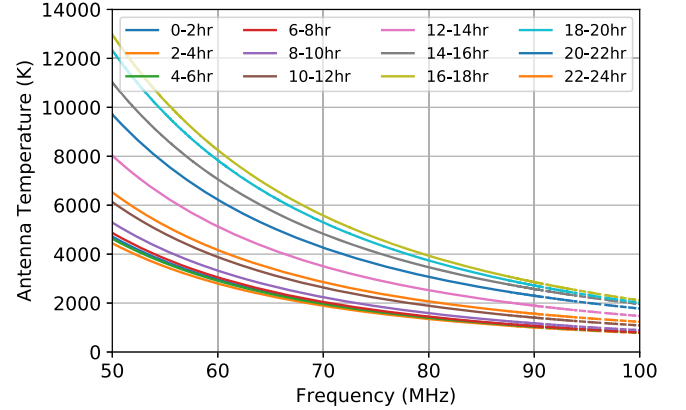

Figure 13. Observed antenna temperature as a function of frequency for the EDGES low-band instrument with a 10 m × 10 m ground plane. Data are binned by LST into two-hour blocks. Some spectral channels between 90 and 100 MHz are omitted to avoid radio frequency interference.

(Monsalve et al. 2017a; Bowman et al. 2018). However, the main analysis here is carried out by comparing the observed spectra without any attempt to compensate for the chromatic beam effects to the simulated spectra obtained using the beam models. In order to provide the cleanest comparison possible, we omit daytime data and include only times when the Sun is at least 10° below the horizon in order to avoid solar emission and reduce ionospheric interference. The processed data from each day are binned into two-hour blocks in LST and the data from all days were averaged together within their respective bins. The resulting binned spectra are shown in Figure 13.

For comparison to the data, we created simulated spectra following the method described in Section 2.3 using both the FEKO and the CST-I beam solutions. We averaged them into the same two-hour LST blocks as the data. To quickly validate the accuracy of the simulated spectra, we compare their predicted antenna temperatures at 75 MHz to the data in
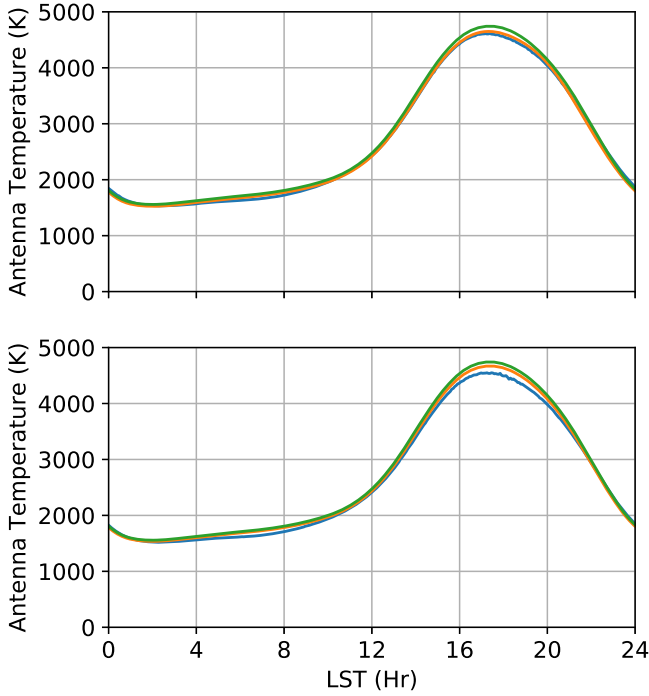
Figure 14. Antenna temperature at 75 MHz as a function of LST for the observed data (blue), simulated spectra using FEKO beam patterns (green), and simulated spectra using CST-I beam patterns (orange). The top panel is for the 10 m × 10 m ground-plane case and the bottom panel is for the extended ground plane.

Figure 14. The disagreement between the simulated spectra and the data varies with LST and is seen to be within 2% and 4% for the 10 m × 10 m and extended ground planes, respectively. To see how well the spectra simulated using the beam models capture the low-level spectral structure in the observations, we fit the same five-term LinLog foreground model described in Equation (5) to the data and to the simulated spectra. We carry out the fitting over the frequency range of 55–97 MHz and then compare the residuals. This frequency band covers all the analysis cases carried out in Bowman et al. (2018). In Figure 15, we show the 10 m × 10 m ground-plane case. Looking across all LST bins, the residuals to the simulated spectra generally follow the trends seen in the residuals to the observations. They are high when the Galactic center is in the beam and gradually decrease as the Galactic center moves to the horizon and below. The residuals in both cases reach a minimum (∼100 mK) when the Galactic center is below the horizon. Within each LST bin, we see that the residuals to the two simulated sky spectra capture the spectral variation of the observation residuals well in terms of the phase of the peaks and troughs. We see the most significant disagreement between the data residuals and simulated residuals in the LST bin of 20–22 hr. This is attributed to the fact that the bright Galactic Center is in the portion of the beam where the gain is changing most rapidly. An error in the beam model is likely to have its strongest effect in the places where the gain changes most rapidly, both in frequency and in angle. This can be seen in Figure 10 between 35° and 60° elevation, where the derivative of the gain of the antenna varies the most with frequency. The differences between the simulated spectra and data are largest for the LSTs on either side of the Galactic Center transiting, but at 16–18 hr, the agreement is good again because the Galactic center is in the slowly changing center of the beam. The bottom
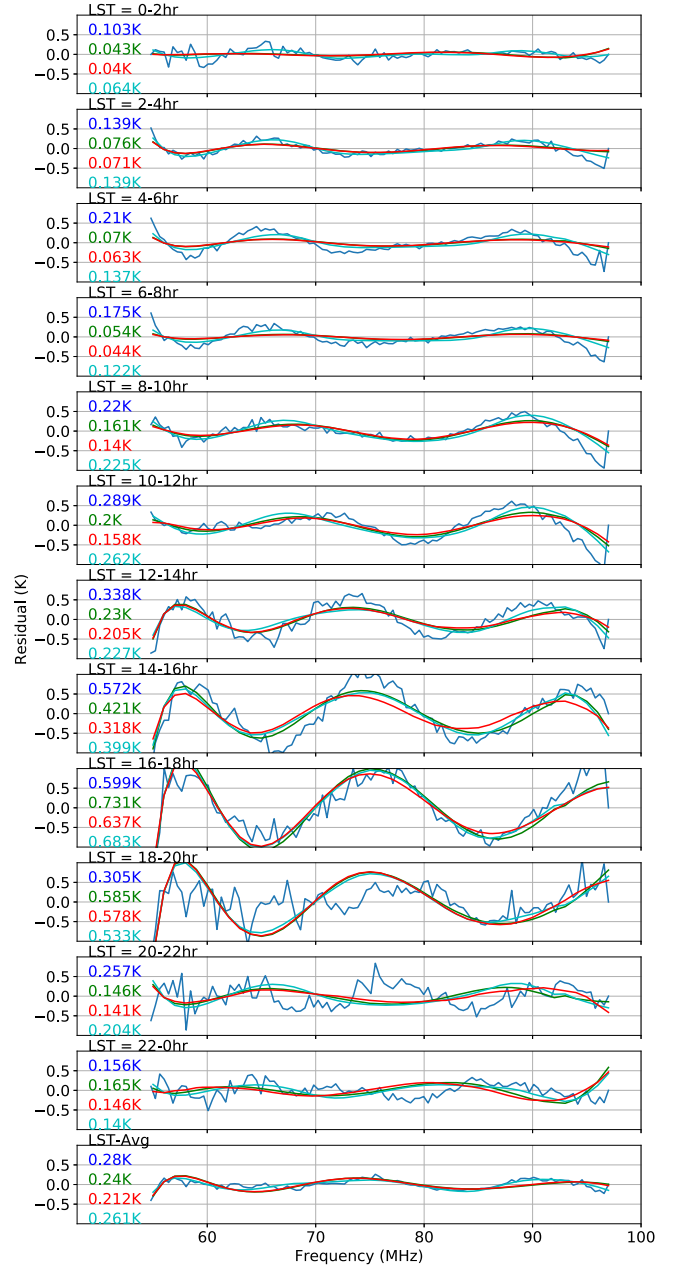

Figure 15. Residuals from the 10 m × 10 m ground plane after fitting and removing a five-term LinLog model to the data and the simulated data for each LST bin. Each row corresponds to a different LST bin and shows the residuals to the data (blue), simulated data using the FEKO beam model (green), simulated data using the CST-I beam model (red), and simulated data including the absorption feature using the FEKO beam model (cyan). The values displayed for each row indicate the FoM derived from the rms of the residuals between 55 and 97 MHz. The bottom row shows the residuals to the full 24 hr averages of the data and simulated data. The values listed for the bottom row are the LST-average FoMs, which differ slightly from the rms of the average data because they are the average of the rms values from each of the LST bins.

plot in Figure 15 is the LST average of all the residuals over the 24 hr. The average residuals align well between the simulations and observations. The FoM in the final subplot is the LST-averaged FoM as used in Table 2. The fractional difference between the FoMs from the simulations and the data is ≈15% for the FEKO solutions and ≈24% for the CST-I solutions.

In Figure 16, we make a similar comparison of the low-level residuals for the extended ground plane. For this ground plane, the worst-case residuals in the bins around Galactic Center
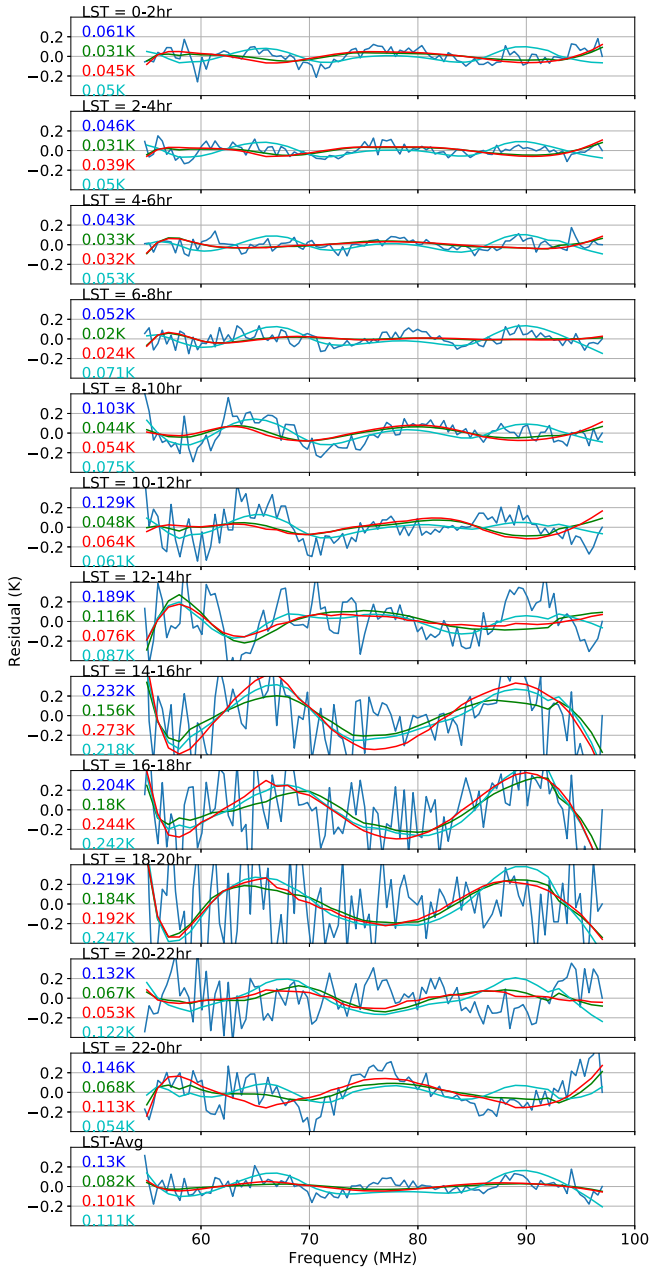
Figure 16. Same as Figure 15, but for the extended ground-plane case.

noise of the data (which is ≈75 mK) in quadrature to the simulated residuals, we still find a 14% unaccountable difference between the residuals. The data residuals tend to have more structure around 65 and 90 MHz compared to the simulations. In the average residual plot we see a larger rms of the residuals from the data than from the simulated spectra.

4.3.1. Beam Correction

When analyzing EDGES data for 21 cm model constraints, we typically apply a beam correction factor to the observed spectra to compensate for the chromatic beam effects. We follow the procedure described in Mozdzen et al. (2019) to calculate a frequency-dependent multiplicative factor that adjusts the measured spectrum to yield an estimate of what would have been observed if the beam were perfectly achromatic. In this paper we add to the comparisons the FoMs after correcting for beam chromaticity in both the simulations and the data. To calculate the beam correction factor, we use our same sky model and the simulated beam patterns found by the FEKO solver. Applying this correction and repeating the FoM calculation serves as a useful additional verification of the performance of the modeled beam patterns. If we have perfect sky and beam models, the beam correction should return the measured spectrum to its intrinsic smooth spectral shape, reducing the FoM.

In Table 2 we show the FoM values for beam-corrected observations. As a reference check, we apply the beam correction first to the simulated observations. For the FEKO simulated observations, we expect that the beam correction should remove all chromatic structures introduced by the beam because the factor is derived from the same underlying model as the simulated observations. Table 2 shows that this is indeed the case. Applying the beam correction to the actual data, we find that it reduces the FoM for the 10 m × 10 m ground plane from 280 mK to 187 mK, an improvement of 33%. This provides further evidence that the simulated beam pattern reproduces some of the structures in the beam of the actual deployed antenna. For the extended ground plane, which already has a comparatively low FoM of 130 mK, the improvement from beam correction is 8%. Our simple sky model may be partly limiting the performance of the beam correction factor.

4.3.2. Sky Model with Absorption Feature

While it is not our goal in this work to fully forward model all aspects of the observations, here we do a simple check of including the absorption feature we reported in Bowman et al. (2018) in our sky model. We model the absorption feature as a flattened Gaussian using the equation for $T_{21}(\nu)$ from the Methods section of Bowman et al. (2018). We use the parameter values of $\nu_0 = 78$ MHz, $\tau = 7$, $w = 18$ MHz, and $A = 500$ mK and add the spectral shape as a global contribution to our sky model. We include these simulated spectra in Figures 15 and 16.

For the 10 m × 10 m ground plane, the residuals after foreground model subtraction are sufficiently large that the addition of the absorption feature has only a minor effect. In the case of the extended ground plane, the addition of the absorption feature leads to a residual spectral structure that better tracks the data in several LST bins. In general it seems to help more at 65 MHz than at 90 MHz. Including the absorption

transit (LST 16–20 hr) have decreased to ∼220 mK compared to ∼560 mK for the 10 m × 10 m case. And during the low-foreground times, the residuals have reduced to ∼45 mK compared to ∼130 mK from the 10 m × 10 m case. We see similar trends in the residual levels as the Galactic center moves in and out of the beam, with the most structure when the Galactic center is nearly overhead and the worst agreement between simulation and observation when it is around 45° elevation (LST 14–16 hr and 20–22 hr). In the extended ground-plane case, overall, we see better agreement between data and simulation. Not only are the residuals lower, but the model seems to do a better job matching the data. This is possibly because the soil electrical properties (which are difficult to know exactly) are less of an influence here. At this level, however, we see that the simulated spectra fail to capture all of the spectral features that are evident in the observation residuals. For the 24 hr average, even after adding the thermal

feature improves the agreement of the LST-averaged FoM between the simulations and data. The difference reduces to 15% compared to 37% when not including the feature. If we add to the simulations thermal noise of similar amplitude as in the data, the agreement further improves to 3% (a difference of only 3.8 mK). We note that in Bowman et al. (2018), we also recovered the absorption feature in fits to data averaged over 6 to 18 hr GHA with no beam corrections applied.

4.3.3. Confirmation of Soil Properties

All simulations of the antenna that included real soil beneath the ground plane had the soil modeled as a lossy dielectric medium with a relative permittivity (ϵ_r) of 3.5 and conductivity (σ) of 0.02 S m^{-1}. These are the values for MRO soil reported by Sutinjo et al. (2015). Here we test these electrical properties of the soil by comparing simulated spectra generated with different soil parameter values against the observations. For this comparison, we return to the FEKO simulation and the observations with the 10 m × 10 m ground plane because the beam patterns for the smaller ground plane are more sensitive to the soil properties than for the extended ground plane.

We perform two grid searches of the soil parameters. We first vary the relative permittivity from 2.5 to 5 in steps of 0.5, keeping the conductivity constant at 0.02 S m^{-1}, and generate simulated spectra for each of the five different beam solutions. Following the usual procedure, these spectra are binned in LST, and a five-term LinLog model is fitted and removed to obtain the residuals. The residuals of the observations and simulated spectra are averaged over 24 hr. The difference between the residuals from the data and simulated observations is plotted in Figure 17. The rms of these second-order residuals are indicated in the top panel of the figure to show which value of the soil properties captures the structure in the data residuals. We next repeat the process, varying the conductivity from 0.001 to 0.1 S m^{-1} and keeping the permittivity constant at 3.5. The results of this grid search are shown in the bottom panel of Figure 17. In the figure we see that the simulations are sensitive to the values of the soil parameters. In the top panel, we see that the beam model is not very sensitive to the relative permittivity. Still, $\epsilon_r = 3.5$ produces one of the best agreements and lowest rms across frequency. For conductivity, the curves between 0.005 and 0.02 S m^{-1} show the best agreement across frequency. Although 0.005 S m^{-1} produces a lower rms, the residuals at lower frequencies are larger. We conclude that the soil properties from Sutinjo et al. (2015) are representative of the conditions seen by EDGES.

5. Discussion

The Cosmic Dawn era is a treasure trove of information of the first stars and early structures in the universe. The redshifted 21 cm line of neutral hydrogen is the most direct probe of this period, but experiments face many challenges. One of the main challenges for global 21 cm experiments is separating the signal from systematics, particularly those caused by the chromaticity of the antenna beam pattern mixing angular sky structure into the observed spectrum. In this paper, we modeled the EDGES low-band antenna beam using different EM solvers and compared their results. The complete EDGES antenna was simulated over an ideal infinite PEC ground and its response was analyzed using the MoM, FEM, and FDTD numerical techniques. We found an agreement of within 25% between
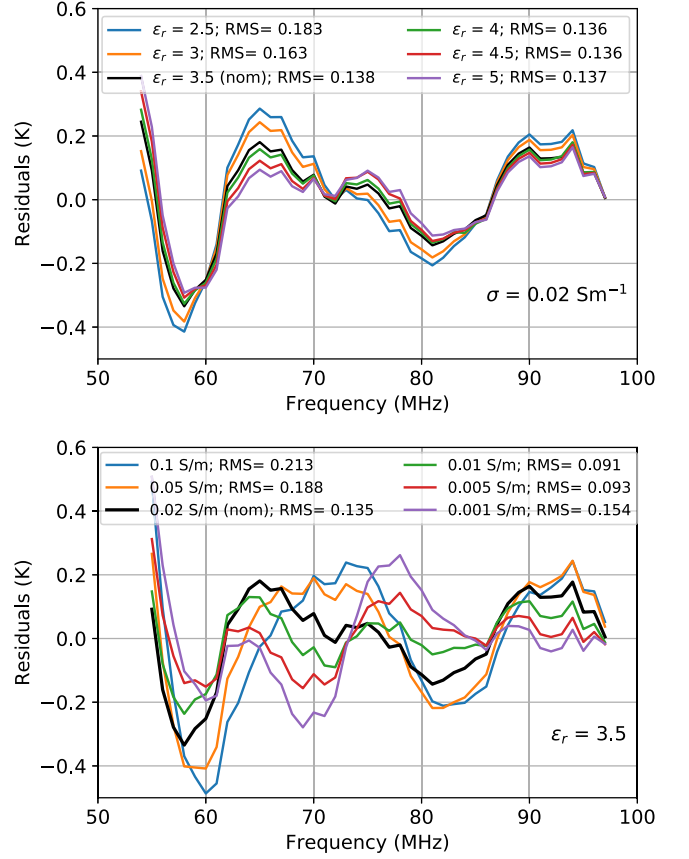

Figure 17. Differences between residuals of the simulated and observed data as a function of frequency. The different spectra are generated by varying the soil's relative permittivity (top) and conductivity (bottom). The residuals of the data and simulated spectra are obtained by fitting a five-term LinLog foreground model. The data and beam solutions used in these plots are from the 10 m × 10 m ground-plane system.

four out of the six solutions we computed, which provides reasonable confidence that the calculated beam is not sensitive to the solver technique used. We then simulated the beams for realistic models of the antenna with the real soil properties and the actual finite ground planes used by the instruments. We tested three independent MoM solutions and found an agreement to within 15% for FEKO and CST-I.

Finite ground planes above realistic soil introduce more beam chromaticity than the ideal infinite PEC ground. In the case of the antenna model with a 10 m × 10 m ground plane, the chromaticity is roughly 3.5 times higher than the ideal ground plane as quantified by the FoM of the simulated spectra. Noting that the residuals from the 10 m × 10 m ground plane are relatively large compared to the predicted amplitude of the cosmological signal, we showed that larger ground-plane sizes can reduce the FoM. Simulations of the extended ground plane used by EDGES predict an LST-averaged FoM of 80 mK, which is only ≈15 mK larger than the value for an infinite PEC ground plane and smaller than the amplitude predicted by many models of the 21 cm signature.

To determine if our quantitative analysis of the beam chromaticity captures what we see in our data, we carried out several comparisons. The simulated spectra and sky observations were processed through equivalent pipelines and compared. Simulated drift scans agree with observations within 4% for both ground planes used by EDGES. Additional comparisons were also carried out by fitting the same

foreground models to the data and simulated spectra and inspecting the residuals. The LST-averaged FoM from the simulated spectra for the 10 m × 10 m ground plane is 240 mK, compared to 280 mK from the data. In the case of the extended ground plane, the LST-averaged FoM of the simulated spectra is ≈82 mK and increases to ≈111 mK after including the absorption feature reported in Bowman et al. (2018) in the sky model. This addition improves the agreement with the FoM of 130 mK from the data. We also calculated the FoM for the data and simulated spectra after correcting for the beam chromaticity factor. The FoM of the beam-corrected spectra showed improvement, providing additional verification of the simulated antenna beam models. Lastly, we looked at the effects of the soil electrical properties on the chromaticity and, by comparing our simulations to measured data, found best-fit soil properties consistent with those reported in Sutinjo et al. (2015).
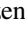
Our ability to characterize the EDGES antenna beam chromaticity is coupled to our knowledge of the intrinsic foreground sky spectrum by relying on astronomical observations to test the beam models. This work has been an initial step in an iterative process of building models for both the instrument and the sky that are self-consistent. We are pursuing the next level of refinements, both in antenna knowledge and sky knowledge. Monsalve et al. (2021) find scale and offset corrections to the diffuse sky maps by Guzmán et al. (2011) and Landecker & Wielebinski (1970) to better match EDGES observations. Our CSIRO collaborators at the MRO are currently acquiring detailed three-dimensional measurements of the large ground planes under the EDGES antennas so that they may be more accurately included in the FEKO model. This is needed because while the EDGES site is broadly very flat, the ground planes do have undulations and deviations from perfectly planar at the 10 cm level across the 30 m structures. In this manuscript, we have assumed perfectly planar ground planes in the EM models. Ultimately, direct measurement of the antenna beam may be the only way to break the coupled parameter space of the sky and beam models. We aim to deploy the open-hardware ECHO calibration drone system (Jacobs et al. 2017) to measure EDGES antenna beam patterns within the next year as the accuracy of the system continues to improve.

ORCID iDs

Nivedita Mahesh https://orcid.org/0000-0003-2560-8023
Judd D. Bowman https://orcid.org/0000-0002-8475-2036
Thomas J. Mozdzen https://orcid.org/0000-0003-4689-4997
Alan E. E. Rogers https://orcid.org/0000-0003-1941-7458
Raul A. Monsalve https://orcid.org/0000-0002-3287-2327

Steven G. Murray https://orcid.org/0000-0003-3059-3823

References

Ali, Z. S., Parsons, A. R., Zheng, H., et al. 2015, ApJ, 809, 61
Berger, P., Newburgh, L. B., Amiri, M., et al. 2016, Proc. SPIE, 9906, 99060D
Bernardi, G., Zwart, J. T. L., Price, D., et al. 2016, MNRAS, 461, 2847
Bowman, J. 2018, http://loco.lab.asu.edu/memos/
Bowman, J. D., Cairns, I., Kaplan, D. L., et al. 2013, PASA, 30, e031
Bowman, J. D., & Rogers, A. E. 2010, Natur, 468, 796
Bowman, J. D., Rogers, A. E., Monsalve, R. A., Mozdzen, T. J., & Mahesh, N. 2018, Natur, 555, 67
Bowman, J. D., Rogers, A. E. E., & Hewitt, J. N. 2008, ApJ, 676, 1
Bradley, R. F., Tauscher, K., Rapetti, D., & Burns, J. O. 2019, ApJ, 874, 153
Chang, C., Monstein, C., Refregier, A., et al. 2015, PASP, 127, 1131
DeBoer, D. R., Parsons, A. R., Aguirre, J. E., et al. 2017, PASP, 129, 045001
Eastwood, M. W., Anderson, M. M., Monroe, R. M., et al. 2019, AJ, 158, 84
Fan, X., Carilli, C., & Keating, B. 2006, ARA&A, 44, 415
Field, G. B. 1958, PIRE, 46, 240
Godara, L. 2018, Handbook of Antennas in Wireless Communications (Boca Raton, FL: CRC Press) https://books.google.com/books?id=qH50DwAAQBAJ
Guzmán, A. E., May, J., Alvarez, H., & Maeda, K. 2011, A&A, 525, A138
Harrington, R. 1993, Field Computation by Moment Method (New York: IEEE Press)
Haslam, C. G. T., Salter, C. J., Stoffel, H., & Wilson, W. E. 1982, A&AS, 47, 1
Hills, R., Kulkarni, G., Meerburg, P. D., & Puchwein, E. 2018, Natur, 564, E32
Hinshaw, G., Larson, D., Komatsu, E., et al. 2013, ApJS, 208, 19
Jacobs, D. C., Burba, J., Bowman, J. D., et al. 2017, PASP, 129, 035002
Landecker, T. L., & Wielebinski, R. 1970, AuJPA, 16, 1
Line, J. L. B., McKinley, B., Rasti, J., et al. 2018, PASA, 35, 45
McGreer, I. D., Mesinger, A., & D'Odorico, V. 2014, MNRAS, 447, 499
Meng Donglin, X. M., & Li, H. 2015, in IEEE 6th Int. Symp., Microwave, Antenna, Propagation, and EMC Technologies (MAPE) (New York: IEEE), 245
Monsalve, R. A., Fialkov, A., Bowman, J. D., et al. 2019, ApJ, 875, 67
Monsalve, R. A., Greig, B., Bowman, J. D., et al. 2018, ApJ, 863, 11
Monsalve, R. A., Rogers, A. E. E., Bowman, J. D., et al. 2021, ApJ, 908, 145
Monsalve, R. A., Rogers, A. E. E., Bowman, J. D., & Mozdzen, T. J. 2017a, ApJ, 847, 64
Monsalve, R. A., Rogers, A. E. E., Bowman, J. D., & Mozdzen, T. J. 2017b, ApJ, 835, 49
Mozdzen, T. J., Bowman, J. D., Monsalve, R. A., & Rogers, A. E. E. 2016, MNRAS, 455, 3890
Mozdzen, T. J., Bowman, J. D., Monsalve, R. A., & Rogers, A. E. E. 2017, MNRAS, 464, 4995
Mozdzen, T. J., Mahesh, N., Monsalve, R. A., Rogers, A. E. E., & Bowman, J. D. 2019, MNRAS, 483, 4411
Neben, A. R., Bradley, R. F., Hewitt, J. N., et al. 2015, RaSc, 50, 614
Nhan, B., Bradley, R. F., & Burns, J. O. 2018, AAS Meeting, 232, 102.04
Oliner, A. A., Jackson, D. R., & Volakis, J. L. 2007, Antenna Engineering Handbook (New York: McGraw-Hill)
Paciga, G., Chang, T.-C., Gupta, Y., et al. 2011, MNRAS, 413, 1174
Patra, N., Subrahmanyan, R., Raghunathan, A., & Udaya Shankar, N. 2013, ExA, 36, 319
Philip, L., Abdurashidova, Z., Chiang, H. C., et al. 2019, JAI, 8, 1950004
Planck Collaboration, Ade, P. A. R., Aghanim, N., et al. 2016, A&A, 594, A13
Pober, J. C., Ali, Z. S., Parsons, A. R., et al. 2015, ApJ, 809, 62
Pober, J. C., Parsons, A. R., Jacobs, D. C., et al. 2012, AJ, 143, 53
Pupillo, G., Naldi, G., Bianchi, G., et al. 2015, ExA, 39, 405
Rafique, M. Z., Cao, Q., & Lian, Z. 2019, in IEEE Int. Conf. on Computational Electromagnetics (ICCEM) (New York: IEEE), 1
Roberts, W. K. 1957, Proc. IRE, 45, 1628
Schneider, R. N., Okoniewski, M. M., & Turner, L. E. 2002, in IEEE MTT-S Int. Microwave Symp. Digest, Vol. 2 (New York: IEEE), 875
Shaver, P. A., Windhorst, R. A., Madau, P., & de Bruyn, A. G. 1999, A&A, 345, 380
Sims, P. H., & Pober, J. C. 2020, MNRAS, 492, 22
Singh, S., Subrahmanyan, R., Shankar, N. U., et al. 2018, ExA, 45, 269
Singh, S., Subrahmanyan, R., Udaya Shankar, N., et al. 2017, ApJL, 845, L12
Sokolowski, M., Tremblay, S. E., Wayth, R. B., et al. 2015, PASA, 32, e004
Spinelli, M., Bernardi, G., & Santos, M. G. 2019, MNRAS, 489, 4007
Sullivan, D. M. 2013, Electromagnetic Simulation Using the FDTD Method (New York: Wiley)
Sutinjo, A. T., Colegate, T. M., Wayth, R. B., et al. 2015, ITAP, 63, 5433
Tingay, S. J., Goeke, R., Bowman, J. D., et al. 2013, PASA, 30, e007

van Haarlem, M. P., Wise, M. W., Gunst, A. W., et al. 2013, A&A, 556, A2

Virone, G., Lingua, A. M., Piras, M., et al. 2014, IAWPL, 13, 169

Wouthuysen, S. A. 1952, AJ, 57, 31

Zahn, O., Reichardt, C. L., Shaw, L., et al. 2012, ApJ, 756, 65

Zheng, Q., Wu, X.-P., Johnston-Hollitt, M., hua Gu, J., & Xu, H. 2016, ApJ, 832, 190

Zheng, Z.-Y., Wang, J., Rhoads, J., et al. 2017, ApJL, 842, L22

Zienkiewicz, O. C., Taylor, R. L., Nithiarasu, P., & Zhu, J. 1977, The Finite Element Method (London: McGraw-Hill)